



www.acsnano.org

# Chip-Scalable, Room-Temperature, Zero-Bias, Graphene-Based Terahertz Detectors with Nanosecond Response Time

Mahdi Asgari, Elisa Riccardi, Osman Balci, Domenico De Fazio, Sachin M. Shinde, Jincan Zhang, Sandro Mignuzzi, Frank H. L. Koppens, Andrea C. Ferrari, Leonardo Viti, and Miriam S. Vitiello\*



Cite This: ACS Nano 2021, 15, 17966–17976

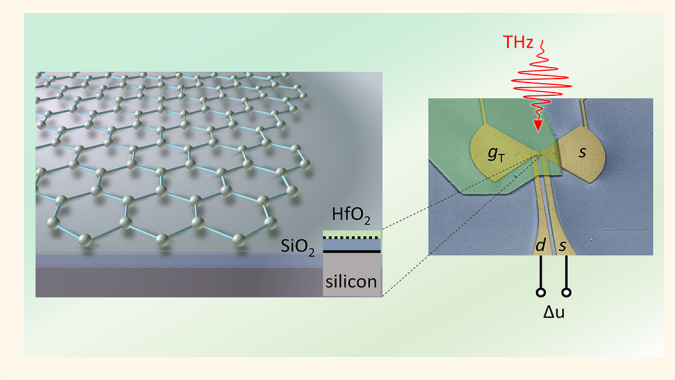


ACCESS

Metrics & More

Article Recommendations

ABSTRACT: The scalable synthesis and transfer of large-area graphene underpins the development of nanoscale photonic devices ideal for new applications in a variety of fields, ranging from biotechnology, to wearable sensors for healthcare and motion detection, to quantum transport, communications, and metrology. We report room-temperature zero-bias thermoelectric photodetectors, based on single- and polycrystal graphene grown by chemical vapor deposition (CVD), tunable over the whole terahertz range (0.1–10 THz) by selecting the resonance of an on-chip patterned nanoantenna. Efficient light detection with noise equivalent powers <1 nWHz<sup>-1/2</sup> and response time ~5 ns at room temperature are demonstrated. This combination of specifications is orders of magnitude better



than any previous CVD graphene photoreceiver operating in the sub-THz and THz range. These state-of-the-art performances and the possibility of upscaling to multipixel architectures on complementary metal-oxide-semiconductor platforms are the starting points for the realization of cost-effective THz cameras in a frequency range still not covered by commercially available microbolometer arrays.

KEYWORDS: photodetectors, graphene, terahertz, nanophotonics, chemical vapor deposition

# INTRODUCTION

Terahertz (THz) radiation (30–300 μm) lies in the infrared region of the electromagnetic spectrum located between microwaves (300 MHz to 300 GHz) and visible (430–770 THz) and is appealing for a number of applications¹ in astrophysics,² high-resolution spectroscopy,³ biomedical imaging,⁴ security,⁵ wireless communications,⁶ and quantum science.⁻ A key requirement is the development of an industrial-scale, reliable, inexpensive production process, not yet achieved for devices operating at THz frequencies, due to the lack of high-volume, wafer-scale, and low-cost technologies.

The advent of grain-of-rice-size THz lasers on a chip, operating at 250 K, a temperature reachable with a plug-in cooler, and chip-scale THz frequency combs will trigger the development of compact and technologically relevant THz systems. However, producing low-cost (<10k \$) and scalable multipixel THz detectors operating at room temperature (RT), with noise equivalent powers (NEP) < 1 nWHz  $^{-1/2}$ , suitable for real-time detection or quantum applications, is still elusive,

in particular for operating frequencies >2THz, appealing for broadband integrated systems comprising miniaturized quantum cascade laser (QCL) combs.<sup>9</sup>

Focal plane arrays, the most commonly employed architectures for multipixel imaging, are currently based on either microbolometers  $^{10}$  or complementary metal-oxide-semiconductor (CMOS) image sensors. Commercially available microbolometers have a low NEP  $\sim 30~\rm pWHz^{-1/2},^{10}$  with a slow response time ( $\tau$ ) in the range  $\sim \! 10 - \! 1000~\mu s.^{10,11}$  CMOS-based field effect transistors (FETs) show  $\tau < 1~\mu s^{12}$  and their NEP decreases (63 pWHz $^{-1/2}$  at 2.5 THz) when reducing the gate lengths to 90 nm.  $^{13}$  However, this hampers

Received: July 28, 2021 Accepted: October 12, 2021 Published: October 27, 2021





the device cost-effectiveness, in particular, for high (>2.5 THz) frequencies. <sup>13</sup>

An option to overcome these limitations is to integrate largearea (cm<sup>2</sup>) single-layer graphene (SLG) with existing CMOS readout integrated circuit (ROIC) architectures, 14,15 taking advantage of well-established, high-volume, and low-cost silicon technology. Graphene-CMOS integration is now feasible thanks to the progress in scalable SLG production and transfer. 15-23 Broadband image sensor arrays operating from ultraviolet (4-400 nm) to short-wave infrared (SWIR, 900-2000 nm) have been realized by integrating large-area CVD graphene with CMOS. 14 The integration of CVD SLG with lithium niobate, a thermally polarizable material, resulted in mid-infrared pyroelectric bolometers with state-of-the-art temperature coefficient of resistance.<sup>24</sup> Single-crystal (SC) CVD SLG, coupled to photonic waveguides, was used for ultrafast, zero-dark-current telecom photodetectors (PDs) for datacoms,<sup>25</sup> and wafer-scale integration of electro-absorption modulators with state-of-the-art performance employing ~12 000 SC SLG flakes was also achieved. 17

The hot-carrier-assisted photothermoelectric effect (PTE) is a very efficient detection mechanism in SLG.  $^{26-31}$  Efficient carrier heating, which stems from the low  $(1.2 \times 10^{11} \ \mathrm{J}\ \mathrm{m}^{-2}\ \mathrm{K}^{-1}$  at 50 mK $^{32}$ ) specific heat of SLG's electrons and high SLG optical phonon energy ( $\sim$ 0.2 eV $^{33}$ ), can result in large electronic temperature gradients ( $\Delta T_{\rm e} \sim 1000 \ \mathrm{K}^{34}$ ) under photoexcitation, pushing  $T_{\rm e}$  far above the lattice temperature. The ultrafast electron dynamics, combined with the absence of a bandgap, enables broadband and high-speed PTE detection. Unlike photovoltaic or bolometric effects, PTE can be activated in asymmetrically coupled FETs $^{29}$  under zero-bias operation (i.e., zero dark current), thus ensuring low power consumption and flicker noise.  $^{39}$ 

In a FET designed to operate as a detector, at THz frequencies, CVD SLG can help to relax the geometrical and technical constraints (e.g., gate length  $\leq$ 90 nm<sup>13</sup>) while preserving compatibility with wafer-level scalable CMOS technology.

Single-pixel PTE-GPDs, based on high-mobility ( $\mu$  up to 53.000 cm² V<sup>-1</sup> s<sup>-1</sup>) graphene encapsulated in hexagonal boron nitride (hBN), are the state-of-the-art when it comes to RT THz and mid-infrared (MIR) PDs, <sup>28,30,40</sup> when compared to any other commercially available technology. Reference 41 reported millimeter-wave (300–600 GHz) RT GPDs exploiting a cm² area CVD SLG with  $\mu$  < 2000 cm² V<sup>-1</sup> s<sup>-1</sup>. However, the performance in the sub-THz range was well below the state-of-the-art, with NEP  $\sim$  0.5 nWHz<sup>-1/2</sup> at 600 GHz, almost 1 order of magnitude larger than that achieved with micromechanically exfoliated<sup>27</sup> or hBN-encapsulated<sup>28–30</sup> SLG at much larger frequencies ( $\sim$ 3THz), where usually a drop in performance is expected.<sup>27–30</sup> The response time was not reported.<sup>41–43</sup>

Here, we present PTE GPDs operating at 2.8 THz exploiting state-of-the-art large-area ( $\sim 1~{\rm cm}^2$ ) single-crystal CVD SLG, with  $\mu$  ranging from 500 to 20.000 cm $^2$  V $^{-1}$  s $^{-1}$ , combined with a planar antenna, on-chip radiofrequency circuitry, and coplanar striplines (CPS) that reach the bonding pads from the electrodes, through an adiabatically matched transition. We tailor the PTE efficiency by using small active areas (down to 150  $\times$  800 nm $^2$ , defined by the gap between the antenna arms and by the SLG channel width) and a low device resistance ( $R \sim k\Omega$ ),  $^{28}$  while simultaneously lowering the

thermal noise ( $\propto R^{1/2}$ ) that is expected to dominate at RT.<sup>29</sup> Our PTE GPDs show NEP on the order of 1 nWHz<sup>-1/2</sup> and  $\tau \sim 5$  ns, much faster than any commercially available RT microbolometer.<sup>11</sup> When compared to nonscalable GFET detectors, realized with high-mobility (15.000–53.000 cm² V<sup>-1</sup> s<sup>-1</sup>) hBN-encapsulated graphene,<sup>29,30</sup> the NEP reported in this work is 1 order of magnitude larger. We ascribe this to the magnitude of the Seebeck coefficient ( $S_{\rm b}$ ) in CVD SLG, proportional to the PTE photoresponse, which is expected to be significantly smaller ( $\sim 10-50~\mu {\rm VK}^{-144}$ ) than that achieved in exfoliated and hBN-encapsulated SLG (up to 180  $\mu {\rm VK}^{-145}$ ). Growth-level grain-size control,<sup>44</sup> large-area hBN encapsulation,<sup>46</sup> and/or dielectric encapsulation<sup>25</sup> can close this performance gap.

#### **RESULTS AND DISCUSSION**

Device Design and Fabrication. SLG SC and polycrystalline films are grown and transferred on Si (350  $\mu$ m, resistivity >10 000  $\Omega$ ·cm) covered with 285 nm SiO<sub>2</sub>, as discussed in Methods. We employ two growth approaches in order to determine whether the material synthesis method plays a significant role in the GPD performances. We use two architectures, the first based on single-top-gated GFETs, integrated in a planar bow-tie antenna (antenna radius  $R_b$  = 24  $\mu$ m, flare angle  $\alpha = 90^{\circ}$ ), the second relying on a set of splitgate p-n junctions, integrated either in a planar bow-tie, or in a linear dipole antenna (total antenna length  $2R_d = 48 \mu m$ ), Figures 1a,b. The antenna dimensions are selected based on the electromagnetic simulations Figures 1c,d, where we use a commercial finite element method (FEM) software (COM-SOL Multiphysics) to evaluate the electric field enhancement at the center of the antenna, as a function of  $R_b$  and  $R_d$ , when a 2.8 THz wave impinges on the GPDs. We also evaluate the antenna response as a function of impinging radiation frequency, using an antenna half-length of 24  $\mu$ m, identical to that used for the experiments (Figure 1a,b). In the model, the THz wave, polarized parallel to the antenna axis, impinges on the detector from the air side. The simulation results (Figure 1e,f) indicate that the two antenna geometries have different response bandwidths. The calculated percent bandwidth, defined as the ratio between absolute bandwidth and central frequency, 47 is 44% for the bow-tie configuration, and 12.5% for the linear dipole one.

Both geometries (Figures.1a,b) are expected to induce PTE rectification when the sensing element is illuminated by THz radiation, with a different principle. For a single-top-gated system,  $\Delta T_{\rm e}$  is generated, asymmetrically with respect to the GFET channel, in the gap between the bow-tie antenna arms constituted by the source (s) and gate (g) electrodes, and directed toward the source side of the GFET. Simultaneously, a different  $S_b$  is established along the channel, due to the different work functions of metal leads and SLG, producing a charge transfer, with a consequent shift of chemical potential in the SLG area under s and drain (d) electrodes.  $^{48,49}$  Å further  $S_b$ difference can be induced by applying a bias  $(V_g)$  to the topgate electrode. 29 This allows selection of the optimum  $S_b$  to maximize the PTE photoresponse. In the p-n junction architecture, the electronic distribution is symmetrically heated in the area corresponding to the antenna gap. In this case, the voltages applied to the left  $(V_{\rm gL})$  and right  $(V_{\rm gR})$  gates are responsible for creating the required  $S_b$  asymmetry along the channel.

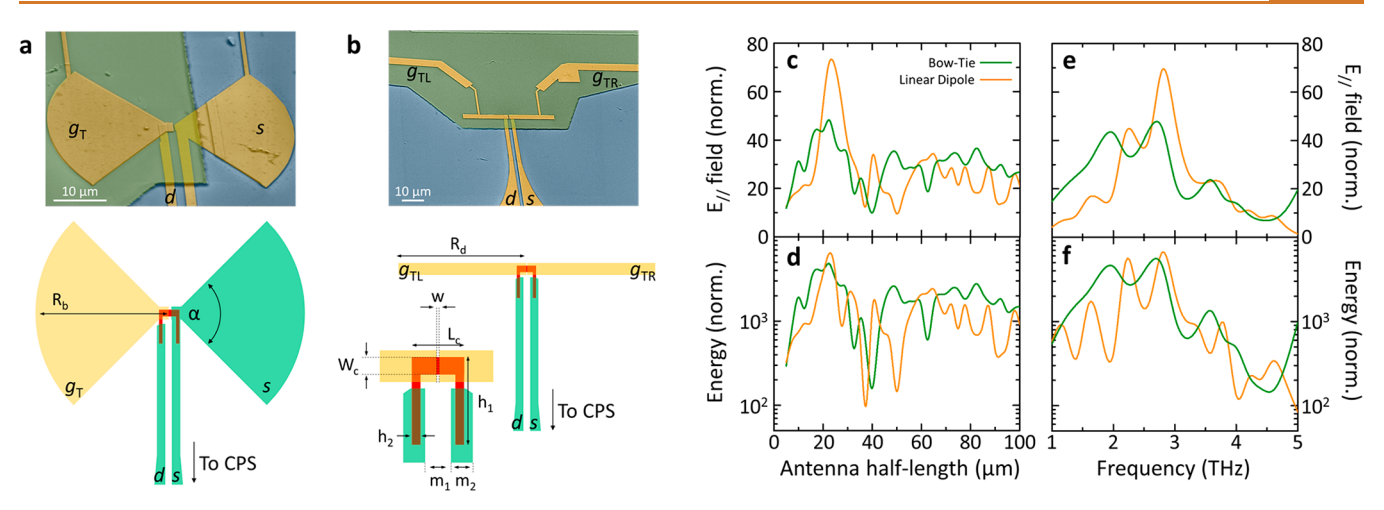


Figure 1. (a) Bow-tie coupled single-gated CVD GFETs, with an on-chip bow-tie antenna.  $R_{\rm b}$  is the antenna radius,  $\alpha=90^{\circ}$  is the flare angle. (b) Dual-gated SLG p-n junction integrated into a linear dipole antenna. The half-length of the dipole,  $R_{\rm d}$ , is indicated. Inset: layout of the p-n junction active element (a similar layout is used for the single-gated geometry) indicating the relevant geometrical parameters.  $L_{\rm c}$  and  $W_{\rm c}$  are the length and width of the gated area, w is the size of the gap between the two top-gates,  $h_{1,2}$  are geometrical parameters defining the contact areas, and  $m_{1,2}$  define the CPS. False color SEM images show two GPDs. (c,d) Antenna simulations showing the field enhancement with respect to the antenna dimensions, for w=200 nm. (c) Enhancement of the electric field component parallel to the antenna axis ( $E_{\parallel}$ ) as a function of the antenna half-length ( $R_{\rm b}$ ,  $R_{\rm d}$ ) under 2.8 THz illumination. (d) Energy enhancement as a function of antenna half-length. The bow-tie antenna has a smaller energy enhancement (a factor  $\sim$ 2). (e) Energy enhancement as a function of radiation frequency. The percent bandwidth is 44% for the bow-tie antenna and 12.5% for the linear dipole antenna. (f) In-plane field enhancement for bow-tie and linear dipole antennas vs frequency. The results in (c,d,e,f) are obtained by evaluating a volume integral in the position of the GFET channel for both energy and in-plane electric field when the metallic antenna is on the substrate and normalized to the case of no antenna on the substrate.

For all GPDs, we employ a common channel geometry, with channel length  $L_c = 4 \mu m$ . We vary the channel width  $W_c$ between 0.8 and 1.8  $\mu$ m. The transferred large (cm<sup>2</sup>) area SLG is etched in O<sub>2</sub> plasma to realize electron beam lithography (EBL) patterned U-shaped structures to increase the SLGmetal interface at the s and d electrodes (Figure 1). This shape is chosen to avoid geometric overlap between top-gates and underlying electrodes, thus allowing the use of a thin (40 nm) oxide film as gate dielectric, maximizing the gate-to-channel capacitance per unit area  $(C_{Ga})$ , while reducing leakage currents and the chance of dielectric breakdown. The SLG channels are annealed in Ar at 280 °C for 2 h before starting the fabrication of the devices. This step reduces the p-doping, leading to reduction of intrinsic charge carrier density,  $n_0$ , from  $5 \times 10^{12}$  to  $0.5 \times 10^{12}$  cm<sup>-2</sup> with respect to non-annealed samples without degrading the material quality.<sup>44</sup> The s and d contacts are then realized by EBL and Cr/Au thermal evaporation (5/100 nm). The top-gate oxide layer (HfO<sub>2</sub>, thickness  $t_{ox}$  = 40 nm) is lithographically defined and grown by atomic layer deposition (ALD) in an OpAL reactor (Oxford Instruments). Considering the permittivity of Hafnium oxide  $\varepsilon_{\rm r}$ = 19.8, 43 the resulting gate-to-channel capacitance per unit area is  $C_{\rm Ga} = \varepsilon_{\rm r} \varepsilon_0 / t_{\rm ox} \sim 0.44 \ \mu \rm F \ cm^{-2}$ . ALD is used because of its compatibility with wafer-scale processing. The top-gates are then defined by EBL and established by metallization (5/100 nm Cr/Au) and lift-off. Scanning electron micrograph (SEM) images of two GPDs are in Figure 1a,b, together with a summary of the relevant geometrical parameters.

**Single Gate GFETs.** We then test the transport properties of the devices. From the characterization of the channel resistance (R) curve as a function of  $V_g$ , we extract the field-effect mobility  $(\mu_{\rm FE})$ , the contact resistance  $(R_0)$  and  $n_0$  by using the fit function  $R = R_0 + (L_{\rm C}/W_{\rm C})(1/n_{\rm 2d}e\mu_{\rm FE})$ , where  $n_{\rm 2d}$  is the gate-dependent charge density, given by  $n_{\rm 2d} = \{n_0^2 + n_{\rm 2d}^2 + n_$ 

 $[C_{Ga}/e (V_G - CNP)]^2\}^{1/2}$ . Figure 2a plots  $R(V_g)$  for one of the single-top-gated bow-tie GPDs. The e/h branch asymmetry with respect to the CNP can be ascribed to their different scattering cross section in the vicinity of charged impurities.<sup>51</sup>

Using the GFET transconductance, it is possible to determine the physical mechanism underlying THz detection. In particular, we numerically evaluate the expected dependence of the photovoltage as a function of  $V_{\rm g}$  in the cases of a detection dominated by the PTE or by the overdamped plasma wave (OPW) mechanisms. In the PTE case, the photovoltage amplitude  $(V_{PTE})$  is proportional to the electronic temperature gradient along the graphene channel  $(\Delta T_e)$ , and its dependence with respect to  $V_{\rm g}$  is determined by the difference between the Seebeck coefficients of the gated  $(S_{bg})$  and ungated  $(S_{bu})$  portions of the channel:  $^{29}$   $V_{PTE} = \Delta T_e \cdot (S_{bg} - S_{bg})$  $S_{bu}$ ).  $S_{b}$  can be extracted from  $R(V_{g})$  (Figure 2a) by using the Mott equation.<sup>29</sup> In FETs operating at room temperature, the OPW mechanism typically interplays with the PTE response, and their individual contributions are often not easy to disentangle in single-gated geometries.<sup>52</sup> However, the dependence of the OPW response  $(V_{\mathrm{OPW}})$  with respect to  $V_{\mathrm{g}}$ slightly differs from the PTE one. In particular, it is proportional to the F-factor of the FET, defined as  $^{52}$  F = $-1/\sigma \times \partial \sigma/\partial V_g$ , where  $\sigma$  is the static conductivity of the FET channel. For GFETs, both F and V<sub>OPW</sub> cross zero at the charge neutrality point (CNP)<sup>29,52</sup> and are expected to be negative for n-doping and positive for p-doping. 29,52 The curves in Figure 2b are calculated from  $R(V_g)$  (Figure 2a) and represent a direct comparison of the two mechanisms for the single-gated device. Importantly, the PTE mechanism entails a double sign change of the photovoltage in proximity of the Dirac point,<sup>29</sup> not expected in the plasma wave effect.<sup>52</sup>

The optical response of the GPDs is then tested using a quantum cascade laser (QCL) at 2.8 THz, with a maximum

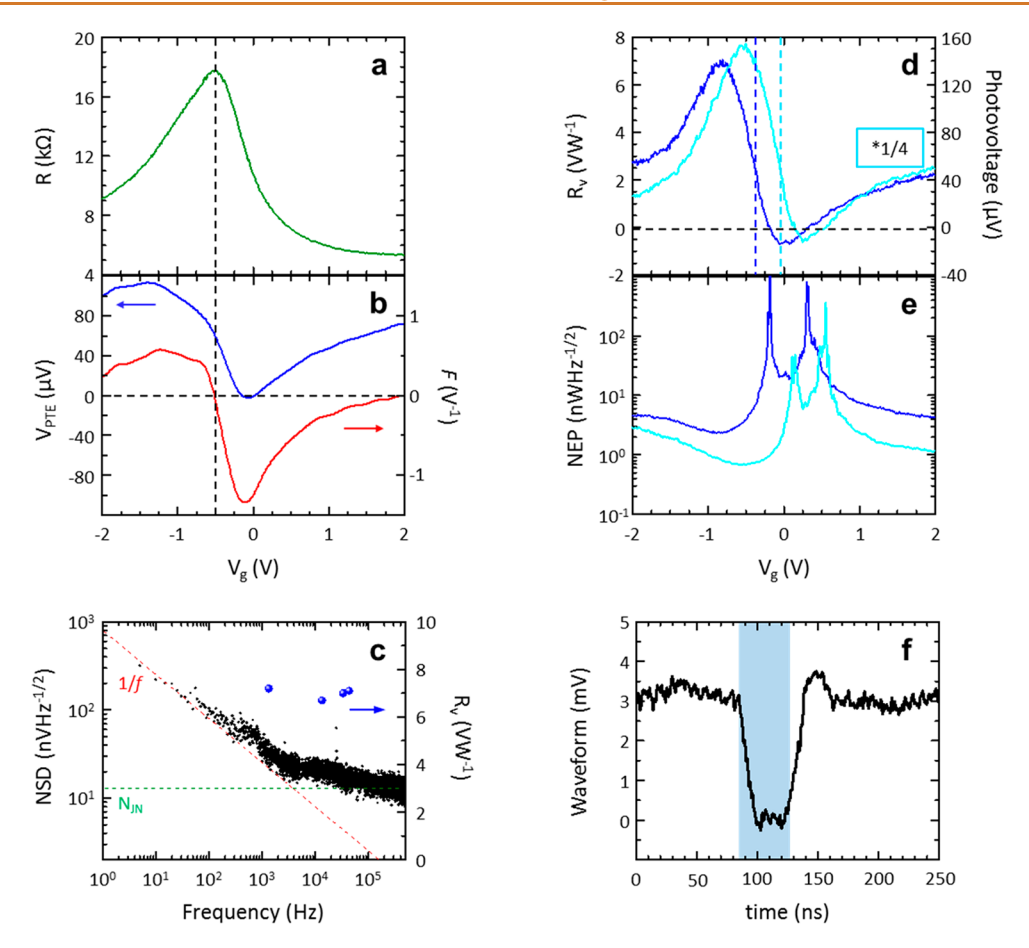


Figure 2. (a) Channel resistance at RT as a function of  $V_g$ , showing the CNP at  $V_g = -0.48$  V. For this device, we extrapolate an electron (hole)  $\mu_{\rm FE} \sim 1200~{\rm cm^2~V^{-1}~s^{-1}}$  (900 cm² V<sup>-1</sup> s<sup>-1</sup>) and  $n_0 \sim 4.1 \times 10^{11}~{\rm cm^{-2}}$ . (b) Comparison between PTE and OPW models. Left vertical axis, blue curve: PTE photovoltage ( $V_{\rm PTE}$ ) obtained as the difference between the Seebeck coefficients under the gate electrode ( $S_{\rm bg}$ ) and in the ungated portion of the channel ( $S_{\rm bu}$ ), multiplied by  $\Delta T_e = 1$  K.  $S_{\rm bg}$  is calculated from the GFET transconductance, using the Mott equation. So  $S_{\rm bu}$  is assumed equal to  $S_{\rm bg}$  at  $V_g = 0$  V. Right vertical axis, red curve: FET factor (F), calculated from the GFET transconductance. Coefficients vertical axis,  $V_g = 0$  V) and air-side maximum responsivity (right vertical axis,  $V_g = -0.6$  V) as a function of frequency. (d) Left vertical axis: THz responsivity measured with a modulation frequency of 1.334 kHz. The double sign change is compatible with a PTE-dominated response. Right vertical axis: photovoltage measured when light impinges from the front and through a Si-lens substrate as a function of  $V_g$ . The improved optical coupling raises the photoresponse by a factor  $\sim$ 4. (e) NEP as a function of  $V_g$ . (f) Black curve: photovoltage time trace recorded when the QCL is driven in the negative differential resistance regime. From the waveform, we extract  $\tau \sim 6 \pm 0.3$  ns. The blue shaded area represents the time interval in which the laser emission is off.

average output power ~1 mW (see Methods).<sup>29</sup> We measure the photovoltage with a lock-in amplifier and calculate the voltage responsivity,  $R_v$  (Figure 2c,d), defined as the measured electric signal divided by incoming radiation power; see Methods. Figure 2d is the  $V_g$  dependent  $R_v$ , collected while the QCL illuminates the detector from the air-side (blue curve). The sign of  $R_v$  changes twice across the  $V_g$  sweep, in agreement with previous findings on PTE-GFET THz GPDs. 28-30 We then collect the photoresponse when the QCL radiation impinges on the GPD from the substrate. This gives a photovoltage increase of a factor ~4 (light-blue curve, Figure 2d), ascribed to the increased directivity of the bow-tie antenna toward the substrate. 53 The comparison between Figure 2b and the experimental responsivity in Figure 2d clearly shows that the measured photoresponse is dominated by the PTE mechanism and cannot be generated by a dominant OPW effect.

We estimate the gate bias dependent NEP (Figure 2e), defined as the ratio between the GPD noise spectral density (NSD, noise voltage per unit bandwidth) and  $R_v$ . We

approximate the NSD with the Johnson–Nyquist noise  $^{28,29}$   $N_{\rm JN}=(\langle V_{\rm th}^{\ 2}\rangle)^{1/2}=(4k_{\rm B}RT)^{1/2},$  where  $k_{\rm B}$  is the Boltzmann constant and T=300 K is the heat sink temperature. In order to prove the validity of this approximation, we directly measure the GPD NSD using a spectrum analyzer (Figure 2c). At low frequencies (<1 kHz), the noise figure is dominated by the contribution of the flicker (1/f) noise, in agreement with ref 39. Above 5 kHz, the 1/f noise becomes negligible and noise is instead dominated by  $N_{\rm JN}$ . Figure 2c plots  $R_{\rm v}$  for QCL modulation frequencies 1.334 to 43.33 kHz (see Methods), demonstrating that  $R_{\rm v}$  is independent of modulation frequency, in this range. The NEP as a function of  $V_{\rm g}$  is in Figure 2e with a minimum  $\sim 3$  nWHz $^{-1/2}$  for air-side illumination and  $\sim 600$  pWHz $^{-1/2}$  when illuminated from the substrate.

The method used for the characterization of the response time is the same as in refs 28-30 for THz detectors and in ref 38 for mid-IR detectors. When the pulsed QCL is operated in the negative differential resistance (NDR) regime, its emission becomes intermittent, and transitions between off and on states occur with rise and fall times  $\sim 1$  ns.  $^{29,30}$  Thus, the

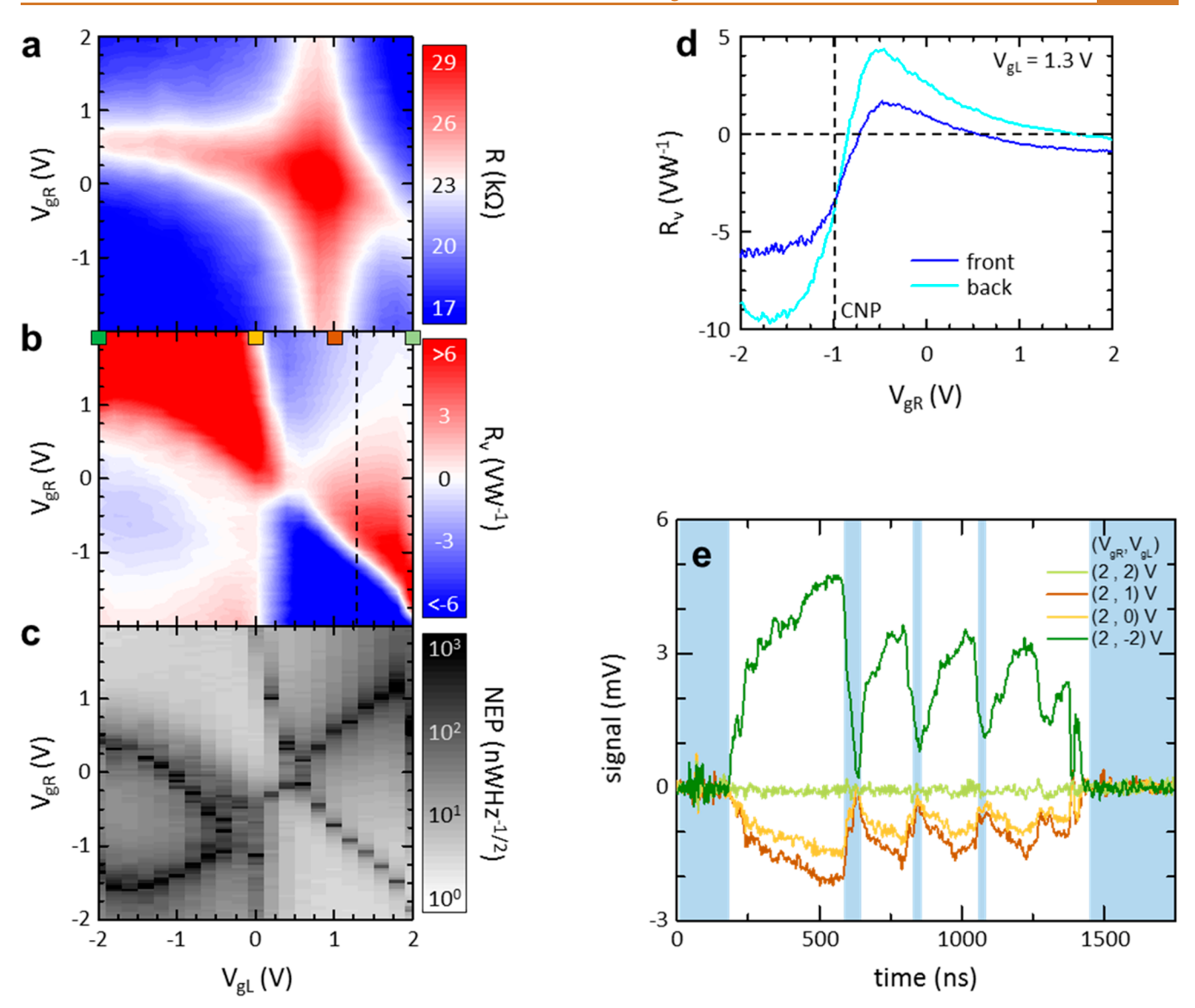


Figure 3. (a) Channel resistance map as a function of the bias applied to the split-gates. Transport regimes corresponding to p-n, p-p, n-p, and n-n doping are seen. (b)  $R_{\rm V}$  map. Sign reversal leads to additional p-p' and n-n' regions, thus a sixfold symmetry, the hallmark of PTE.<sup>54</sup> Colored squares indicate the voltage configurations in which the waveforms in (e) were recorded. The dashed vertical line indicates the line-cut in the map corresponding to (d). (c) NEP map, showing a minimum ~1.3 nWHz<sup>-1/2</sup> for  $V_{\rm gL} = -2$  V,  $V_{\rm gR} = 1.7$  V. (d) Responsivity measured while irradiating the detector from substrate side (light-blue) and air side (blue), keeping  $V_{\rm gL} = 1.3$  V and while sweeping  $V_{\rm gR}$  from -2 V to +2 V. (e) Photovoltage time traces, recorded when the QCL is driven in the negative differential resistance regime, measured for different  $V_{\rm gL}$ ,  $V_{\rm gR}$ . The extracted  $\tau$  is  $\sim$ 5.2  $\pm$  0.4 ns. Shaded areas mark the time intervals where the laser output power is expected to vanish as a consequence of fluctuations.

dynamics of the source are faster than those of the GPDs, and the intensity fluctuations can then be used to estimate the receiver response time. We then drive the QCL in pulsed mode in the NDR state. The GPD output is preamplified and monitored with a fast oscilloscope, with readout bandwidth = 1.1 GHz (see Methods). The setup allows us to evaluate detector  $\tau \sim 1$  ns or larger (anything faster than that would be setup-limited). Figure 2f shows one of the QCL intensity fluctuations (on–off–on) retrieved by a single-gated GFET for  $V_{\rm g} = -0.5$  V, giving  $\tau \sim 6 \pm 0.3$  ns.

**PN Junction Devices.** We then characterize the *p-n* junction devices by collecting resistance (Figure 3a) and  $R_{\rm V}$  (Figure 3b) while sweeping  $V_{\rm gL}$  and  $V_{\rm gR}$ .

(Figure 3b) while sweeping  $V_{\rm gL}$  and  $V_{\rm gR}$ . The field effect is visible in the resistance map (Figure 3a) of a representative p-n junction GPD, showing 4 regions, corresponding to the different doping in the two sides of the junction. Considering a horizontal line cut across the map of R and using the fitting procedure described in ref 50 gives  $\mu_{\rm FE}(e)$  = 480 cm<sup>2</sup> V<sup>-1</sup> s<sup>-1</sup>,  $\mu_{\rm FE}(h)$  = 1080 cm<sup>2</sup> V<sup>-1</sup> s<sup>-1</sup>, and  $n_0$  = 5 ×  $10^{11}$  cm<sup>-2</sup>.

We then measure the  $R_{\rm V}$  map by illuminating the sample from the air-side. In the case of hot-carrier-assisted photo-detection, the photoresponse is proportional to the  $S_{\rm b}$  difference in the two differently doped regions of the junction. As a consequence of the non-monotonic nature of  $S_{\rm b}$ , the photovoltage exhibits multiple sign switches, resulting in the characteristic sixfold pattern (Figure 3b), the signature of PTE-driven detection. Under the assumption of a NSD dominated by thermal fluctuations (Johnson–Nyquist noise), we extract NEP following the procedure described before, reaching  $\sim 1.3$ 

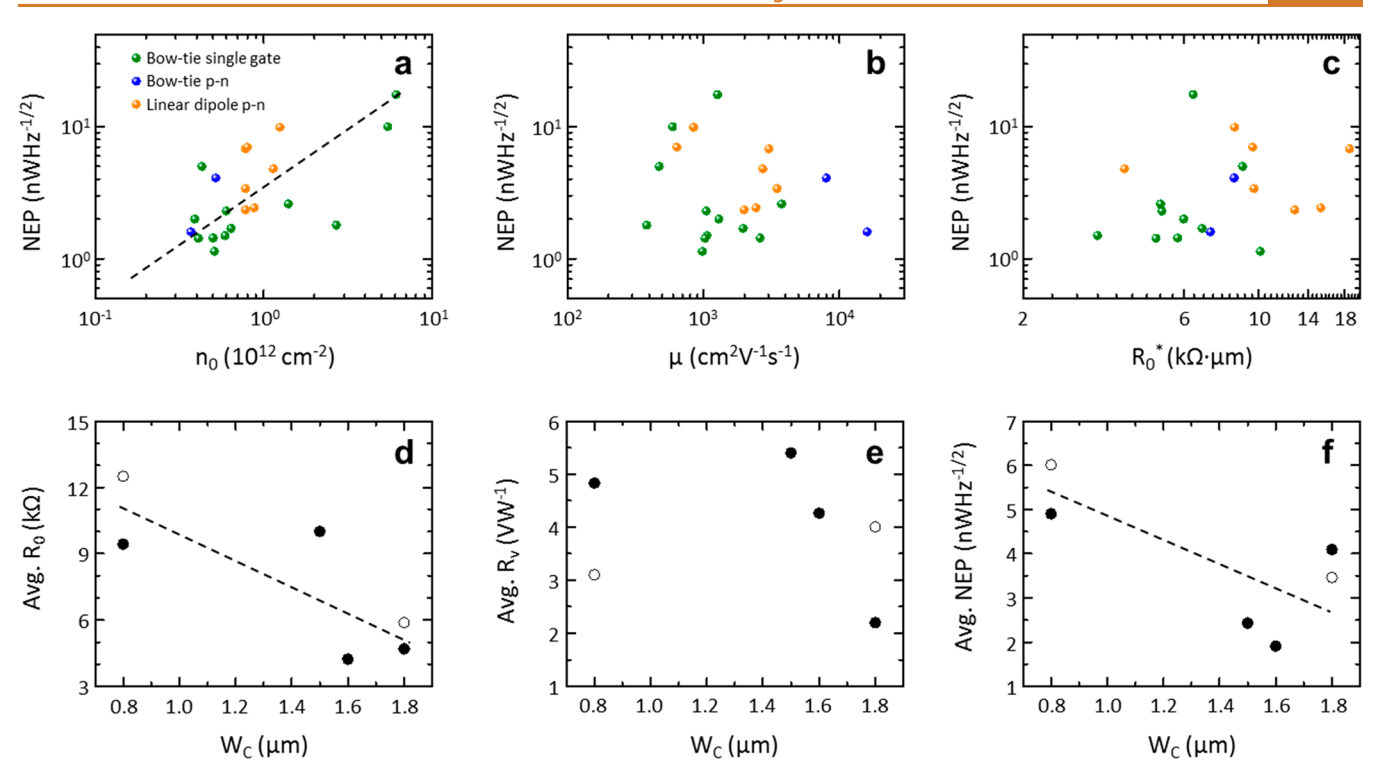


Figure 4. (a) Scatter plot of NEP (for air-side illumination) as a function of  $n_0$ . The dashed black line is a guide for the eye. Green points represent single-top-gated GFETs; yellow (blue) points indicate split-gate p-n junctions equipped with a linear dipole (bow-tie) antenna. (b) NEP  $vs \mu$ . (c) NEP  $vs R_0^*$ . (d-f) Device performance plotted as a function of  $W_c$ . Filled circles represent single top-gated GFETs, open circles p-n junction GPDs. (d) Average contact resistance. (e) Average  $R_v$ . (f) Average NEP. Averages are calculated for each  $W_c$  and GPD type.

nWHz<sup>-1/2</sup> for  $V_{\rm gL} = -2$  V,  $V_{\rm gR} = 1.7$  V, which defines a p-n junction at the geometrical center of the SLG channel. The NEP map inherits the sixfold pattern of the  $R_{\rm v}$  map (Figure 3c). Figure 3d presents a comparison between the responsivity measured when the p-n junction GPD is illuminated from the air-side and from the substrate, showing an increase of a factor of  $\sim$ 2 in the latter case, in agreement with the expected increase in the antenna directivity toward the Si substrate. S5

We then characterize  $\tau$  of the p-n junction devices, in analogy with the single-gated GFETs. Figure 3d plots the time traces of the optical response recorded for a representative GPD, for different gate configurations, while driving the QCL in the NDR regime. In agreement with the sixfold patterns, the signal waveforms have different signs, corresponding to different  $S_{\rm b}$  on the left and right sides of the junction. For example, when  $V_{\rm gL}=V_{\rm gR}=2$  V, the signal drops to zero, because  $S_{\rm b}$  does not change across the junction. By fitting the measured time traces, we extract a minimum  $\tau\sim5.2\pm0.4$  ns for  $V_{\rm gL}=2$  V,  $V_{\rm gR}=-2$  V, i.e., when the p-n junction is activated

We then investigate 25 GPDs fabricated following the two architectures described above. Among them, 4 were not working properly and showed NEP > 10  $\mu$ WHz<sup>-1/2</sup> and are not considered in the following discussion. This gives a yield of >80%. The scatter plot of the minimum NEP as a function of  $n_0$  (Figure 4a) shows a positive correlation between the two quantities, with a Pearson correlation coefficient (see Methods),  $\rho_{\rm p} \sim 0.8$ . Therefore, a lower SLG doping is desirable to improve NEP. On the other hand, the scatter plot of the minimum NEP as a function of  $\mu$  has a negligible correlation  $\rho_{\rm p} = -0.2$  (Figure 4b). Similarly, the contact resistance  $R_0^*=R_0W_{\rm c}$  plays a minor role in determining the

NEP ( $\rho_p = 0.1$ , Figure 4c), with respect to  $n_0$ , which appears to be the dominant electrical factor in the optical performance. This can be intuitively related with the PTE mechanism.  $n_{0}$ , which depends on the material quality, affects the magnitude of  $S_{\rm b}$ . Beside this,  $\Delta T_{\rm e}$  is larger for lower  $n_0$ , because the heat capacity is smaller. Lower  $n_0$  gives a lower NEP.<sup>28</sup> Since, from our findings, the dependence between NEP and  $\mu$  is much weaker,  $n_0$  is the decisive electrical parameter in the PTE-GPD performance. Figure 4a shows similar performance between GPDs with bow-tie or linear dipole antennas, consistent with the numerical simulations of Figure 1. Single-gated GFETs show a slightly better NEP (a factor ~2 lower, on average) with respect to split-gate architectures. This makes single-gated GFETs more promising for the realization of large arrays of detectors, being easier to fabricate and more practical to operate, with only one electrode to be biased. A detailed statistical analysis of the device-to-device variability of optoelectronic parameters is reported in the Methods section.

By analyzing the effect of  $W_c$  (0.8–2  $\mu$ m) on the detection performance, we conclude that, even though the dependence is weak, the NEP increases for narrower channels (Figure 4f) as a consequence of the increased device resistance (Figure 4d) that translates to an increase of NSD, not fully counterbalanced by  $R_V$ , Figure 4e.

# **CONCLUSIONS**

We prepared antenna-coupled GPDs operating at 2.8 THz exploiting large-area single-crystal and polycrystalline CVD graphene. These combine high sensitivity (with a low NEP  $\sim$  nWHz<sup>-1/2</sup>) and low response time ( $\sim$ 5 ns), enabled by the combination of PTE with fast readout electronics and on-chip

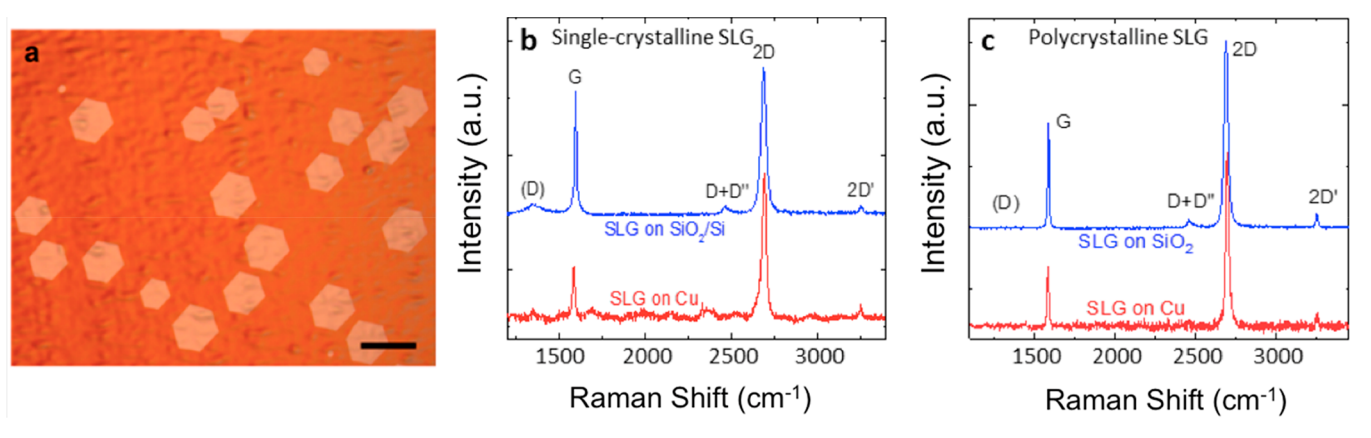


Figure 5. (a) Representative optical image of SLG grains grown on Cu, with contrast enhanced by heating in air for 1 min at 250 °C. <sup>58</sup> Scale bar 100  $\mu$ m. (b) Representative Raman spectra, measured at 532 nm of as-grown SLG SC on Cu (blue) and SLG after transfer on SiO<sub>2</sub>/Si (red). (c) Raman spectra at 514.5 nm of polycrystalline SLG as grown (red) on Cu and transferred SLG (blue) on SiO<sub>2</sub>/Si.

high bandwidth architectures. These performances make them competitive with other room-temperature technologies operating in the 3-6 THz range.  $^{10-13}$  Zero-bias, zero-power consumption PTE detectors provide an advantage to meet the requirements of low cost and low SWaP (size, weight, and power) of room-temperature THz cameras. The broadband nature of the PTE rectification can be exploited for multifrequency detecting platforms. Optimization of thermoelectric properties could be achieved by transferring SLG on alternative dielectrics 25,56 to reduce the residual carrier concentration at the charge neutrality point and bring S<sub>b</sub> in the 100  $\mu$ V K<sup>-1</sup> range. The dielectric environment can affect the charge inhomogeneity and the residual carrier concentration at the charge neutrality point, which, in turn, has an influence on the Seebeck coefficient (and NEP as demonstrated in Figure 4a). This correlation stems from the resulting graphene quality and from the different densities of free and trapped charges in the different substrates. 25,56 The possibility to combine scalable large-area CVD graphene with large-area scalable hBN, in scalable heterostructures, promises significant performance improvements. Large-scale integration could be achieved by implementing a technological flowchart fully compatible with standard CMOS readout integrated circuits.

# **METHODS**

Graphene Growth and Transfer. SLG SCs are grown via CVD on Cu, Figure 5a, in an Aixtron Black Magic on 35-µm-thick Cu foil, electropolished using a solution containing 57 450 mL deionized (DI) water, 225 mL ortho-phosphoric acid 85% (H<sub>3</sub>PO<sub>4</sub>), 225 mL ethanol, 45 mL isopropanol, and 7.2 g urea. 60 mL of this solution is poured in a staining jar. Next, a Cu foil is placed in the filled jar and connected to the positive terminal of a current generator. A thicker (~0.7 mm) Cu plate is placed in the jar parallel to the Cu foil at a distance  $\sim 2.5$ cm and connected to the negative terminal of the current generator. A current ~1.5A is then passed for 90 s to smooth and clean the Cu foil surface. The foil is then loaded in the furnace to perform the CVD growth<sup>58</sup> by raising T from RT to  $\sim$ 1000 °C in Ar. The pressure is kept constant ~25 mbar throughout the whole process. These conditions are then held for 30 min to anneal the Cu foil. 50 sccm H<sub>2</sub> and 30 sccm 0.01% diluted CH<sub>4</sub> in Ar are then added to the chamber to trigger the growth of SLG, which lasts ~3 h. The sample is then cooled to RT and unloaded from the furnace. A4-950 K poly(methyl methacrylate) polymer (PMMA) is spin-coated at 4000 rpm on the SLG+Cu surface. This is then placed on a solution of 3 g of ammonium persulfate in 100 mL DI water to etch Cu. Once Cu is etched, PMMA+SLG is transferred to a beaker with DI water for rinsing and then lifted with the target over a Si substrate (350  $\mu$ m,

resistivity >10 000  $\Omega$ cm) covered with SiO<sub>2</sub> (300 nm) and left to dry overnight. This substrate choice is technologically attractive thanks to its scalability and affordability. The PMMA is finally removed with acetone, leaving SLG on SiO<sub>2</sub>/Si.

Raman spectroscopy is performed to monitor the SLG quality<sup>59,60</sup> with a Renishaw inVia spectrometer at 514 and 532 nm and a 100× objective lens. The blue curve in Figure 5b shows the Raman spectrum of SLG on Cu after subtracting the Cu photoluminescence. 61 The single Lorentzian (2D peak) at  $\sim$ 2691.3  $\pm$  0.1 cm<sup>-1</sup> with full-width-at-half-maximum (FWHM) of  $\sim 27.3 \pm 0.4 \text{ cm}^{-1}$  is consistent with SLG. 59,60 The G peak position is  $Pos(G) \sim 1585.1$  $\pm 0.2 \text{ cm}^{-1}$  and FWHM(G)  $\sim 16.4 \pm 0.7 \text{ cm}^{-1}$ . The 2D to G area and intensity ratios are  $A(2D)/A(G) \sim 4.67 \pm 0.22$  and  $I(2D)/I(G) \sim 3.6$ ± 0.4. We then wet-transfer SLG on SiO<sub>2</sub>/Si. Next, we recheck the SLG quality to confirm that this is not affected by the transfer process. The red curve in Figure 5b is a representative Raman spectrum of SLG on SiO<sub>2</sub>/Si. The position of the 2D peak, Pos(2D), is  $\sim$ 2685.3  $\pm$  $0.3 \text{ cm}^{-1}$ , with FWHM(2D) ~36.9 ± 0.2 cm<sup>-1</sup>; Pos(G) ~ 1595.2 ± 0.1 cm<sup>-1</sup>, FWHM(G)  $\sim$  11.8  $\pm$  0.2 cm<sup>-1</sup>. T  $A(2D)/A(G) \sim$  4.39  $\pm$ 0.04,  $I(2D)/I(G) \sim 1.49 \pm 0.08$ . These indicate  $\sim 250 \pm 50$  meV ptype doping. <sup>62,63</sup> The D peak  $\sim 1352.8 \pm 0.6 \text{ cm}^{-1}$  has an intensity ratio with respect to the G peak  $I(D)/I(G) \sim 0.046 \pm 0.003$ , indicating a small defect density of  $\sim\!(1.7\,\pm\,0.4)\times10^{10} cm^{-2.64,65}$ 

Continuous polycrystalline SLG is grown on  $\sim 30-\mu$ m-thick Cu foil by low-pressure CVD (LPCVD). Before growth, the foil is annealed at 1050 °C for 2 h under H<sub>2</sub> (100 sccm) at 1 atm and cooled to RT. For the growth, the system is heated to 1050 °C with 50 sccm H2 at 0.4 Torr, and the Cu foil is annealed for 2 h. 5 sccm CH<sub>4</sub> is introduced to initiate growth, and the CH<sub>4</sub> flow is stopped after 30 min to terminate it. The system is cooled to RT under 50 sccm H2 in 60 min. To transfer SLG, the top side of SLG/Cu is spin-coated with PMMA (A4 950) at 1000 rpm for 60 s. PMMA/SLG/Cu is then baked on hot plate at 80° for 10 min. SLG on the Cu back side is removed by O<sub>2</sub> plasma. Electrochemical delamination is carried out by applying voltage to a Pt anode and PMMA/SLG/Cu cathode in a NaOH aqueous solution (1 M). A voltage potential of 2 V is held in the twoelectrode system. Delamination completes within a few seconds, and the PMMA/SLG stack floats on electrolyte. The stack is then transferred into DI water and scooped out onto SiO<sub>2</sub>/Si, dried overnight, and then baked at 80 °C for 10 min. PMMA is dissolved in acetone. The sample is rinsed in IPA and dried.

As grown and transferred SLG is characterized by Raman spectroscopy. A statistical analysis is performed to estimate doping and defect density. The errors are calculated from the standard deviation across different spectra, the spectrometer resolution ( $\sim$ 1 cm<sup>-1</sup>), and the uncertainty associated with the different methods to estimate the doping from Pos(G), FWHM(G), I(2D)/I(G), A(2D)/A(G), and Pos(2D). The Raman spectrum of as-grown polycrystalline continuous SLG on Cu is in Figure 5c, after Cu PL removal. <sup>59</sup> The 2D

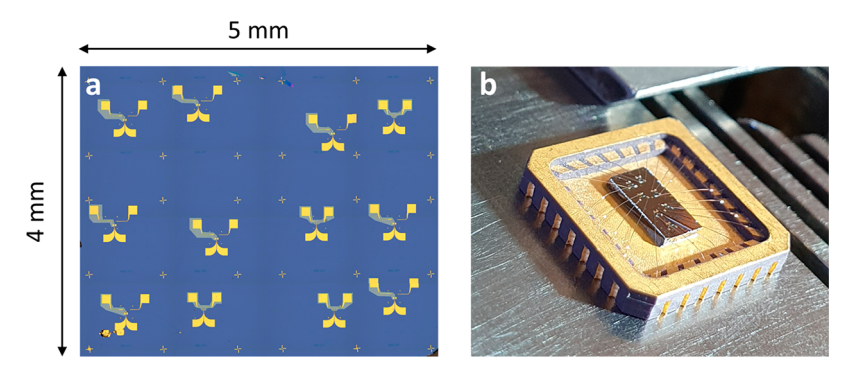


Figure 6. (a) Optical microscope image of 12 devices on Si/SiO<sub>2</sub>. (b) Photograph of a chip mounted on a ceramic carrier for dc electrical characterization.

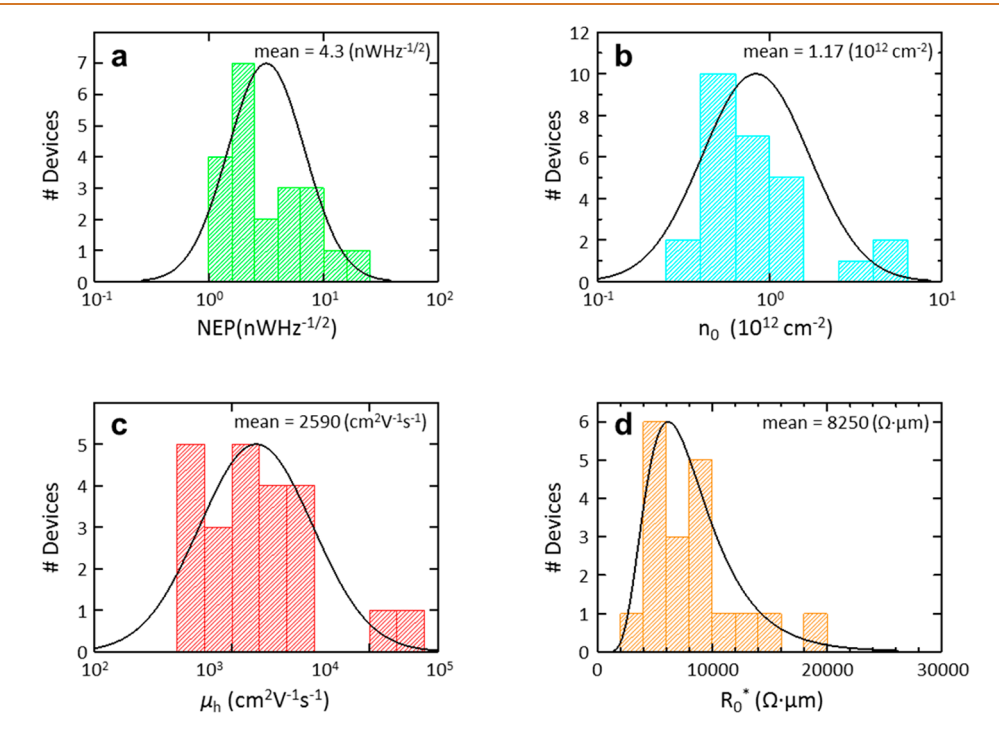


Figure 7. (a) Distribution of NEPs. The solid line represents a fitting normal distribution (note that the x-axis is in log-scale). The calculated mean values and IQR are 4.3 nWHz<sup>-1/2</sup> and 3.3 nWHz<sup>-1/2</sup>, respectively. (b) Distribution of the residual carrier density  $n_0$ , with mean  $\sim 1.17 \times 10^{12}$  cm<sup>-2</sup> and IQR  $\sim 0.63 \times 10^{12}$  cm<sup>-2</sup>. The solid line represents a Gaussian fit to the data. (c) Distribution of  $\mu_{\rm h}$ , with mean  $\sim 2590$  cm<sup>2</sup> V<sup>-1</sup> s<sup>-1</sup> and IQR  $\sim 1780$  cm<sup>2</sup> V<sup>-1</sup> s<sup>-1</sup>. The solid line represents a normal distribution fit to the data. (d) Distribution of contact resistance, with mean  $\sim 8250$   $\Omega$ · $\mu$ m and IQR  $\sim 4530$   $\Omega$ · $\mu$ m. The solid line represents a log-normal distribution function.

peak is a single Lorentzian with FWHM(2D)  $\sim$ 24 ± 3 cm<sup>-1</sup>, signature of SLG. SP Pos(G)  $\sim$  1585 ± 2 cm<sup>-1</sup>, FWHM(G)  $\sim$  16 ± 2 cm<sup>-1</sup>, Pos(2D)  $\sim$  2703 ± 4 cm<sup>-1</sup>,  $I(2D)/I(G) \sim$  3.6 ± 0.4,  $A(2D)/A(G) \sim$  5.5 ± 0.7. No D peak is observed, indicating negligible Raman active defects. So, The 2D peak retains its single-Lorentzian line shape with FWHM(2D)  $\sim$  27 ± 1 cm<sup>-1</sup>, Pos(G)  $\sim$  1591 ± 2 cm<sup>-1</sup>, FWHM(G)  $\sim$  9 ± 2 cm<sup>-1</sup>, Pos(2D)  $\sim$  2691 ± 2 cm<sup>-1</sup>,  $I(2D)/I(G) \sim$  1.6 ± 0.2,  $A(2D)/A(G) \sim$  4.7 ± 0.4, indicating a p-doping with Fermi energy  $E_F \sim$  300 ± 50 meV, corresponding to a carrier concentration  $n_0 \sim$  (5.7 ± 1.8) ×  $10^{12}$  cm<sup>-2</sup>. So,  $n_0 = 10^{12}$  corresponds to a defect density  $n_0 = 10^{12}$  cm<sup>-2</sup> for excitation energy 2.41 eV and  $E_F = 300 \pm 50$  meV.

**Fabrication Details.** Large-area CVD graphene offers the possibility to fabricate multiple devices in parallel. Figure 6a shows 12 GFETs. As-fabricated samples are then mechanically cleaved and mounted on ceramic chip carriers for electrical and optical testing (Figure 6b).

**Optical Characterization.** We employ a 2.8 THz QCL driven in pulsed mode (repetition rate 40 kHz, duty cycle 4%). The laser pulses

are modulated by a square wave envelope with frequency ranging from 1.334 to 43.33 kHz, simultaneously acting as reference for lockin detection. The  $40^{\circ}$  divergent optical beam emitted from the QCL facet is first collimated and then focused by two TPX lenses, reaching a spot-size with FWHM  $\sim$ 300  $\mu$ m. A set of motorized linear stages provides precise positioning of the detector in the focal point. The total power  $P_t$  over a 3  $\times$  5 cm<sup>2</sup> area around the beam spot is measured with an absolute THz power/energy meter (Thomas Keating). Since our GPDs active areas are much smaller than the beam waist, the fraction of optical power delivered to the GPDs,  $P_{st}$  is estimated as  $P_t \times S_t / S_{\lambda}$ , where  $S_t$  is the beam spot area and  $S_{\lambda} = \lambda^2 / 4$  is the diffraction limited area. <sup>29</sup> The photoresponse  $V_{\rm LIA}$  is measured between the s and d electrodes with a lock-in (SR5210) over a voltage preamplifier (dlInstruments) having gain G = 1000. The photovoltage  $\Delta u$  and  $R_V$  are then calculated as  $\Delta u = 2.2 \times V_{LJA}/G$  and  $R_v = \Delta u/P_a$ . au is determined by recording the time traces of  $\Delta u$  with an oscilloscope (Tektronix DPO5204, 2 GHz bandwidth), when the QCL is driven in the negative differential resistance region.<sup>29</sup>  $\Delta u$  is preamplified with a 1.1 GHz amplifier (Femto DUPVA) using a gain of 70 dB. The input impedance of the preamplifier (50  $\Omega$ ) is much smaller than the GFET resistance ( $\sim 10 \text{ k}\Omega$ ), thus producing a signal loss  $\sim 200$  through the corresponding voltage divider.

**Correlation Analysis.** In order to characterize the correlation between our GPDs optical and electrical performances, we use the Pearson (product-moment) correlation coefficient,  $\rho_{\rm p}$ , a measure of the linear correlation between two variables.<sup>67</sup> Given the data sets p and q, each with N observations,  $\rho_{\rm p}$  is defined as<sup>67</sup>

$$\rho_{p}(p, q) = \frac{1}{N-1} \sum_{i=1}^{N} \left( \frac{p_{i} - p'}{\sigma_{p}} \right) \left( \frac{q_{i} - q'}{\sigma_{q}} \right)$$

where p' and q' are the mean values and  $\sigma_p$  and  $\sigma_q$  are the standard deviations for p and q, respectively. As a result,  $\rho_p$  is a value in the range (-1,1), where  $\rho_p=1$   $(\rho_p=-1)$  indicates a positive (negative) linear dependence and  $\rho_p=0$  indicates no linear correlation between the two variables.

**Device-to-Device Performance Variability.** Performance variability is important in view of upscaling the technology to multiple-pixel architectures. <sup>68</sup> Therefore, we evaluate the variability of 4 detector parameters: NEP,  $n_0$ ,  $\mu_b$ , and  $R_0^*$ . These show a normal distribution in logarithmic scale (Figure 7).

We calculate each variable's statistical dispersion as the interquartile range (IQR),  $^{69}$  defined as the difference between the upper and lower quartiles of a data set. The results of this analysis are reported in Figure 7 and show that the detector NEP has a variability  $\sim\!3.3~\rm nWHz^{-1/2}$ , which is a large fraction of the mean NEP (4.3  $\rm nWHz^{-1/2}$ ) and much larger than the minimum NEP (1.1  $\rm nWHz^{-1/2}$ ). The variability of NEP then represents a critical aspect in the future development of multipixel arrays architectures.

#### **AUTHOR INFORMATION**

#### **Corresponding Author**

Miriam S. Vitiello — NEST, CNR - Istituto Nanoscienze and Scuola Normale Superiore, 56127 Pisa, Italy; orcid.org/0000-0002-4914-0421; Email: miriam.vitiello@sns.it

# **Authors**

Mahdi Asgari – NEST, CNR - Istituto Nanoscienze and Scuola Normale Superiore, 56127 Pisa, Italy

Elisa Riccardi – NEST, CNR - Istituto Nanoscienze and Scuola Normale Superiore, 56127 Pisa, Italy

Osman Balci — Cambridge Graphene Centre, University of Cambridge, Cambridge CB3 0FA, United Kingdom;
o orcid.org/0000-0003-2766-2197

**Domenico De Fazio** – ICFO-Institut de Ciencies Fotoniques, 08860 Castelldefels, Barcelona, Spain

Sachin M. Shinde – Cambridge Graphene Centre, University of Cambridge, Cambridge CB3 0FA, United Kingdom

Jincan Zhang – Cambridge Graphene Centre, University of Cambridge, Cambridge CB3 0FA, United Kingdom

Sandro Mignuzzi – Cambridge Graphene Centre, University of Cambridge, Cambridge CB3 0FA, United Kingdom

Frank H. L. Koppens — ICFO-Institut de Ciencies Fotoniques, 08860 Castelldefels, Barcelona, Spain; orcid.org/0000-0001-9764-6120

Andrea C. Ferrari — Cambridge Graphene Centre, University of Cambridge, Cambridge CB3 0FA, United Kingdom

Leonardo Viti — NEST, CNR - Istituto Nanoscienze and Scuola Normale Superiore, 56127 Pisa, Italy; orcid.org/0000-0002-4844-2081

Complete contact information is available at: https://pubs.acs.org/10.1021/acsnano.1c06432

# **Notes**

The authors declare no competing financial interest.

### **ACKNOWLEDGMENTS**

We acknowledge funding from the European Union through the Graphene Flagship, the Marie Curie H2020-MSCA-ITN-2017 TeraApps (765426), and by the European Research Council Grants (681379) SPRINT, Hetero2D, GSYNCOR, EPSRC grants EP/L016087/1, EP/K01711X/1, EP/K017144/1, EP/N010345/1, EP/V000055/1.

#### REFERENCES

- (1) Mittleman, D. M. Twenty Years of Terahertz Imaging. Opt. Express 2018, 26, 9417–9431.
- (2) Echternach, P. M.; Pepper, B. J.; Reck, T.; Bradford, C. M. Single Photon Detection of 1.5 THz Radiation with the Quantum Capacitance Detector. *Nature Astronomy* **2018**, *2*, 90–97.
- (3) Bartalini, S.; Consolino, L.; Cancio, P.; De Natale, P.; Bartolini, P.; Taschin, A.; De Pas, M.; Beere, H.; Ritchie, D.; Vitiello, M. S.; Torre, R. Frequency-Comb-Assisted Terahertz Quantum Cascade Laser Spectroscopy. *Phys. Rev. X* **2014**, *4*, 021006.
- (4) Yang, X.; Zhao, X.; Yang, K.; Liu, Y.; Liu, Y.; Fu, W.; Luo, Y. Biomedical Applications of Terahertz Spectroscopy and Imaging. *Trends Biotechnol.* **2016**, 34, 810–824.
- (5) Federici, J. F.; Schulkin, B.; Huang, F.; Gary, D.; Barat, R.; Oliveira, F.; Zimdars, D. THz Imaging and Sensing for Security Applications Explosives, Weapons and Drugs. *Semicond. Sci. Technol.* **2005**, *20*, S266.
- (6) Ghasempour, Y.; Shrestha, R.; Charous, A.; Knightly, E.; Mittleman, D. M. Single-Shot Link Discovery for Terahertz Wireless Networks. *Nat. Commun.* **2020**, *11*, 2017.
- (7) Yang, X.; Vaswani, C.; Sundahl, C.; Mootz, M.; Luo, L.; Kang, J. H.; Perakis, I. E.; Eom, C. B.; Wang, J. Lightwave-Driven Gapless Superconductivity and Forbidden Quantum Beats by Terahertz Symmetry Breaking. *Nat. Photonics* **2019**, *13*, 707–713.
- (8) Khalatpour, A.; Paulsen, A. K.; Deimert, C.; Wasilewski, Z. R.; Hu, Q. High-Power Portable Terahertz Laser Systems. *Nat. Photonics* **2021**, *15*, 16–20.
- (9) Vitiello, M. S.; Consolino, L.; Inguscio, M.; De Natale, P. Toward New Frontiers for Terahertz Quantum Cascade Laser Frequency Combs. *Nanophotonics* **2020**, *10*, 187–194.
- (10) Simoens, F.; Meilhan, J. Terahertz Real-Time Imaging Uncooled Array Based on Antenna- and Cavity-Coupled Bolometers. *Philos. Trans. R. Soc., A* **2014**, 372, 20130111.
- (11) Sizov, F. Terahertz Radiation Detectors: State-of-the-Art. Semicond. Sci. Technol. 2018, 33, 123001.
- (12) Ikamas, K.; Lisauskas, A.; Boppel, S.; Hu, Q.; Roskos, H. G. Efficient Detection of 3 THz Radiation from Quantum Cascade Laser Using Silicon CMOS Detectors. *J. Infrared, Millimeter, Terahertz Waves* **2017**, *38*, 1183–1188.
- (13) Lisauskas, A.; Bauer, M.; Boppel, S.; Mundt, M.; Khamaisi, B.; Socher, E.; Venckevicius, R.; Minkevicius, L.; Kasalynas, I.; Seliuta, D.; Valusis, G.; Krozer, V.; Roskos, H. G. Exploration of Terahertz Imaging with Silicon MOSFETs. *J. Infrared, Millimeter, Terahertz Waves* **2014**, *35*, 63–80.
- (14) Goossens, S.; Navickaite, G.; Monasterio, C.; Gupta, S.; Piqueras, J. J.; Pérez, R.; Burwell, G.; Nikitskiy, I.; Lasanta, T.; Galán, T.; Puma, E.; Centeno, A.; Pesquera, A.; Zurutuza, A.; Konstantatos, G.; Koppens, F. H. L. Broadband Image Sensor Array Based on Graphene–CMOS Integration. *Nat. Photonics* **2017**, *11*, 366–371.
- (15) Romagnoli, M.; Sorianello, V.; Midrio, M.; Koppens, F. H. L.; Huyghebaert, C.; Neumaier, D.; Galli, P.; Templ, W.; D'Errico, A.; Ferrari, A. C. Graphene-Based Integrated Photonics for Next-Generation Datacom and Telecom. *Nat. Rev. Mater.* **2018**, *3*, 392–414.
- (16) Backes, C.; Abdelkader, A. M.; Alonso, C.; Andrieux-Ledier, A.; Arenal, R.; Azpeitia, J.; Balakrishnan, N.; Banszerus, L.; Barjon, J.; Bartali, R.; Bellani, S.; Berger, C.; Berger, R.; Bernal Ortega, M. M.; Bernard, C.; Beton, P. H.; Beyer, A.; Bianco, A.; Bøggild, P.; Bonaccorso, F.; et al. Production and Processing of Graphene and Related Materials. 2D Mater. 2020, 7, 022001.

- (17) Giambra, M. A.; Mišeikis, V.; Pezzini, S.; Marconi, S.; Montanaro, A.; Fabbri, F.; Sorianello, V.; Ferrari, A. C.; Coletti, C.; Romagnoli, M. Wafer-Scale Integration of Graphene-Based Photonic Devices. *ACS Nano* **2021**, *15*, 3171–3187.
- (18) Cai, J.; Ruffieux, P.; Jaafar, R.; Bieri, M.; Braun, T.; Blankenburg, S.; Muoth, M.; Seitsonen, A. P.; Saleh, M.; Feng, X.; Müllen, K.; Fasel, R. Atomically Precise Bottom-Up Fabrication of Graphene Nanoribbons. *Nature* **2010**, *466*, 470–473.
- (19) Neumann, C.; Kaiser, D.; Mohn, M. J.; Füser, M.; Weber, N.-E.; Reimer, O.; Gölzhäuser, A.; Weimann, T.; Terfort, A.; Kaiser, U.; Turchanin, A. Bottom-Up Synthesis of Graphene Monolayers with Tunable Crystallinity and Porosity. *ACS Nano* **2019**, *13*, 7310–7322.
- (20) Bonaccorso, F.; Lombardo, A.; Hasan, T.; Sun, S.; Colombo, L.; Ferrari, A. C. Production and Processing of Graphene and 2D Crystals. *Mater. Today* **2012**, *15*, 564–589.
- (21) Bae, S.; Kim, H.; Lee, Y.; Xu, X. F.; Park, J. S.; Zheng, Y.; Balakrishnan, J.; Lei, T.; Kim, H. R.; Song, Y. I.; Kim, Y. J.; Kim, K. S.; Ozyilmaz, B.; Ahn, J. H.; Hong, B. H.; Iijima, S. Roll-to-Roll Production of 30-in. Graphene Films for Transparent Electrodes. *Nat. Nanotechnol.* **2010**, *5*, 574.
- (22) Banszerus, L.; Schmitz, M.; Engels, S.; Goldsche, M.; Watanabe, K.; Taniguchi, T.; Beschoten, B.; Stampfer, C. Ballistic Transport Exceeding 28  $\mu$ m in CVD Grown Graphene. *Nano Lett.* **2016**, *16*, 1387–1391.
- (23) De Fazio, D.; Purdie, D. G.; Ott, A. K.; Braeuninger-Weimer, P.; Khodkov, T.; Goossens, S.; Taniguchi, T.; Watanabe, K.; Livreri, P.; Koppens, F. H. L.; Hofmann, S.; Goykhman, I.; Ferrari, A. C.; Lombardo, A. High-Mobility, Wet-Transferred Graphene Grown by Chemical Vapor Deposition. *ACS Nano* **2019**, *13*, 8926–8935.
- (24) Sassi, U.; Parret, R.; Nanot, S.; Bruna, M.; Borini, S.; De Fazio, D.; Zhao, Z.; Lidorikis, E.; Koppens, F. H. L.; Ferrari, A. C.; Colli, A. Graphene-Based Mid-Infrared Room-Temperature Pyroelectric Bolometers with Ultrahigh Temperature Coefficient of Resistance. *Nat. Commun.* 2017, *8*, 14311.
- (25) Miseikis, V.; Marconi, S.; Giambra, M. A.; Montanaro, A.; Martini, L.; Fabbri, F.; Pezzini, S.; Piccinini, G.; Forti, S.; Terrés, B.; Goykhman, I.; Hamidouche, L.; Legagneux, P.; Sorianello, V.; Ferrari, A. C.; Koppens, F. H. L.; Romagnoli, M.; Coletti, C. Ultrafast, Zero-Bias, Graphene Photodetectors with Polymeric Gate Dielectric on Passive Photonic Waveguides. *ACS Nano* **2020**, *14*, 11190–11204.
- (26) Koppens, F. H. L.; Mueller, T.; Avouris, Ph.; Ferrari, A. C.; Vitiello, M. S.; Polini, M. Photodetectors Based on Graphene, Other Two-Dimensional Materials and Hybrid Systems. *Nat. Nanotechnol.* **2014**, *9*, 780–793.
- (27) Cai, X.; Sushkov, A. B.; Suess, R. J.; Jadidi, M. M.; Jenkins, G. S.; Nyakiti, L. O.; Myers-Ward, R. L.; Li, S.; Yan, J.; Gaskill, D. K.; Murphy, T. E.; Drew, H. D.; Fuhrer, M. S. Sensitive Room-Temperature Terahertz Detection *via* the Photothermoelectric Effect in Graphene. *Nat. Nanotechnol.* **2014**, *9*, 814–819.
- (28) Castilla, S.; Terrés, B.; Autore, M.; Viti, L.; Li, J.; Nikitin, A. Y.; Vangelidis, I.; Watanabe, K.; Taniguchi, T.; Lidorikis, E.; Vitiello, M. S.; Hillenbrand, R.; Tielrooij, K.-J.; Koppens, F. H. L. Fast and Sensitive Terahertz Detection Using an Antenna-Integrated Graphene pn Junction. Nano Lett. 2019, 19, 2765–2773.
- (29) Viti, L.; Purdie, D. G.; Lombardo, A.; Ferrari, A. C.; Vitiello, M. S. HBN-Encapsulated, Graphene-Based, Room-Temperature Terahertz Receivers, with High Speed and Low Noise. *Nano Lett.* **2020**, 20, 3169–3177.
- (30) Viti, L.; Cadore, A. R.; Yang, X.; Vorobiev, A.; Muench, J. E.; Watanabe, K.; Taniguchi, T.; Stake, J.; Ferrari, A. C.; Vitiello, M. S. Thermoelectric Graphene Photodetectors with Sub-Nanosecond Response Times at Terahertz Frequencies. *Nanophotonics* **2020**, *10*, 89–98.
- (31) Mittendorff, M.; Winnerl, S.; Murphy, T. E. 2D THz Optoelectronics. Adv. Opt. Mater. 2021, 9, 2001500.
- (32) Kokkoniemi, R.; Girard, J.-P.; Hazra, D.; Laitinen, A.; Govenius, J.; Lake, R. E.; Sallinen, I.; Vesterinen, V.; Partanen, M.; Tan, J. Y.; Chan, K. W.; Tan, K. Y.; Hakonen, P.; Möttönen, M.

- Bolometer Operating at the Threshold for Circuit Quantum Electrodynamics. *Nature* **2020**, *586*, 47–51.
- (33) Piscanec, S.; Lazzeri, M.; Mauri, F.; Ferrari, A. C.; Robertson, J. Kohn Anomalies and Electron-Phonon Interactions in Graphite. *Phys. Rev. Lett.* **2004**, *93*, 185503.
- (34) Soavi, G.; Wang, G.; Rostami, H.; Purdie, D. G.; De Fazio, D.; Ma, T.; Luo, B.; Wang, J.; Ott, A. K.; Yoon, D.; Bourelle, S. A.; Muench, J. E.; Goykhman, I.; Dal Conte, S.; Celebrano, M.; Tomadin, A.; Polini, M.; Cerullo, G.; Ferrari, A. C. Broadband, Electrically Tunable Third-Harmonic Generation in Graphene. *Nat. Nanotechnol.* 2018, 13, 583–588.
- (35) Brida, D.; Tomadin, A.; Manzoni, C.; Kim, Y. I.; Lombardo, A.; Milana, S.; Nair, R. R.; Novoselov, K. S.; Ferrari, A. C.; Cerullo, G.; Polini, M. Ultrafast Collinear Scattering and Carrier Multiplication in Graphene. *Nat. Commun.* **2013**, *4*, 1987.
- (36) Espinosa-Ortega, T.; Luk'yanchuk, I. A.; Rubo, Y. G. Magnetic Properties of Graphene Quantum Dots. *Phys. Rev. B: Condens. Matter Mater. Phys.* **2013**, *87*, 205434.
- (37) Tielrooij, K. J.; Piatowski, L.; Massicotte, M.; Woessner, A.; Ma, Q.; Lee, Y.; Myhro, K. S.; Lau, C. N.; Jarillo-Herrero, P.; van Hulst, N. F.; Koppens, F. H. L. Generation of Photovoltage in Graphene on a Femtosecond Timescale Through Efficient Carrier Heating. *Nat. Nanotechnol.* **2015**, *10*, 437.
- (38) Tielrooij, K.-J.; Hesp, N. C. H.; Principi, A.; Lundeberg, M. B.; Pogna, E. A. A.; Banszerus, L.; Mics, Z.; Massicotte, M.; Schmidt, P.; Davydovskaya, D.; Purdie, D. G.; Goykhman, I.; Soavi, G.; Lombardo, A.; Watanabe, K.; Taniguchi, T.; Bonn, M.; Turchinovich, D.; Stampfer, C.; Ferrari, A. C.; et al. Out-of-Plane Heat Transfer in van der Waals Stacks through Electron—Hyperbolic Phonon Coupling. *Nat. Nanotechnol.* **2018**, *13*, 41.
- (39) Balandin, A. A. Low-Frequency 1/f Noise in Graphene Devices. *Nat. Nanotechnol.* **2013**, *8*, 549–555.
- (40) Castilla, S.; Vangelidis, I.; Pusapati, V.-V.; Goldstein, J.; Autore, M.; Slipchenko, T.; Rajendran, K.; Kim, S.; Watanabe, K.; Taniguchi, T.; Martín-Moreno, L.; Englund, D.; Tielrooij, K.-J.; Hillenbrand, R.; Lidorikis, E.; Koppens, F. H. L. Plasmonic Antenna Coupling to Hyperbolic Phonon-Polaritons for Sensitive and Fast Mid-Infrared Photodetection with Graphene. *Nat. Commun.* **2020**, *11*, 4872.
- (41) Zak, A.; Andersson, M. A.; Bauer, M.; Matukas, J.; Lisauskas, A.; Roskos, H. G.; Stake, J. Antenna-Integrated 0.6 THz FET Direct Detectors Based on CVD Graphene. *Nano Lett.* **2014**, *14*, 5834.
- (42) Bianco, F.; Perenzoni, D.; Convertino, D.; De Bonis, S. L.; Spirito, D.; Perenzoni, M.; Coletti, C.; Vitiello, M. S.; Tredicucci, A. Terahertz Detection by Epitaxial-Graphene Field-Effect-Transistors on Silicon Carbide. *Appl. Phys. Lett.* **2015**, *107*, 131104.
- (43) Bianco, F.; Miseikis, V.; Perenzoni, D.; Coletti, C.; Perenzoni, M.; Tredicucci, A. Antenna-Coupled Graphene Field-Effect Transistors as a Terahertz Imaging Array. *IEEE Trans. Terahertz Sci. Technol.* **2021**, *11*, 70–78.
- (44) Lim, G.; Kihm, K. D.; Kim, H. G.; Lee, W.; Lee, W.; Pyun, K. P.; Cheon, S.; Lee, P.; Min, J. Y.; Ko, S. H. Enhanced Thermoelectric Conversion Efficiency of CVD Graphene with Reduced Grain Sizes. *Nanomaterials* **2018**, *8*, 557.
- (45) Duan, J.; Wang, X.; Lai, X.; Li, G.; Watanabe, K.; Taniguchi, T.; Zebarjadi, M.; Andrei, E. Y. High Thermoelectric Power Factor in G/hBN Devices. *Proc. Natl. Acad. Sci. U. S. A.* **2016**, *113*, 14272–14276.
- (46) Wang, R.; Purdie, D. G.; Fan, Y.; Massabuau, F.C.-P.; Braeuninger-Weimer, P.; Burton, O. J.; Blume, R.; Schloegl, R.; Lombardo, A.; Weatherup, R. S.; Hofmann, S. A Peeling Approach for Integrated Manufacturing of Large Monolayer hBN Crystals. *ACS Nano* **2019**, *13*, 2114–2126.
- (47) Balanis, C. A. Antenna Theory: Analysis and Design, 3rd ed.; John Wiley & Sons, Inc.: Hoboken, NJ, 2005; p 70.
- (48) Giovannetti, G.; Khomyakov, P. A.; Brocks, G.; Karpan, V. M.; van den Brink, J.; Kelly, P. J. Doping Graphene with Metal Contacts. *Phys. Rev. Lett.* **2008**, *101*, 026803.
- (49) Song, S. M.; Park, J. K.; Sul, O. J.; Cho, B. J. Determination of Work Function of Graphene Under a Metal Electrode and Its Role in Contact Resistance. *Nano Lett.* **2012**, *12*, 3887–3892.

- (50) Kim, S.; Nah, J.; Jo, I.; Shahrjerdi, D.; Colombo, L.; Yao, Z.; Tutuc, E.; Banerjee, S. K. Realization of a High Mobility Dual-Gated Graphene Field-Effect Transistor with Al<sub>2</sub>O<sub>3</sub> Dielectric. *Appl. Phys. Lett.* **2009**, *94*, 062107.
- (51) Chen, J.-H.; Jang, C.; Adam, S.; Fuhrer, M. S.; Williams, E. D.; Ishigami, M. Charged-Impurity Scattering in Graphene. *Nat. Phys.* **2008**, *4*, 377–381.
- (52) Bandurin, D. A.; Gayduchenko, I.; Cao, Y.; Moskotin, M.; Principi, A.; Grigorieva, I. V.; Goltsman, G.; Fedorov, G.; Svintsov, D. Dual Origin of Room Temperature Sub-Terahertz Photoresponse in Graphene Field Effect Transistors. *Appl. Phys. Lett.* **2018**, *112*, 141101.
- (53) Jiang, Z.; Wang, Y.; Chen, L.; Yu, Y.; Yuan, S.; Deng, W.; Wang, R.; Wang, Z.; Yan, Q.; Wu, X.; Zhang, X. Antenna-Integrated Silicon—Plasmonic Graphene Sub-Terahertz Emitter. *APL Photon.* **2021**, *6*, 066102.
- (54) Gabor, N. M.; Song, J. C. W.; Ma, Q.; Taychatanapat, T.; Watanabe, K.; Taniguchi, T.; Levitov, L. S.; Jarillo-Herrero, P. Hot Carrier-Assisted Intrinsic Photoresponse in Graphene. *Science* **2011**, 334, 648–652.
- (55) Nguyen, T. K.; Park, I. Resonant Antennas on Semi-Infinite and Lens Substrates at Terahertz Frequency. *Convergence of Terahertz Sciences in Biomedical Systems* **2012**, 181–193.
- (56) Scarfe, S.; Cui, W.; Luican-Mayer, A.; Ménard, J.-M. Systematic THz Study of the Substrate Effect in Limiting the Mobility of Graphene. *Sci. Rep.* **2021**, *11*, 8729.
- (57) Miseikis, V.; Convertino, D.; Mishra, N.; Gemmi, M.; Mashoff, T.; Heun, S.; Haghighian, N.; Bisio, F.; Canepa, M.; Piazza, V.; Coletti, C. Rapid CVD Growth of Millimetre-Sized Single Crystal Graphene Using a Cold-Wall Reactor. 2D Mater. 2015, 2, 014006.
- (58) Braeuninger-Weimer, P.; Brennan, B.; Pollard, A. J.; Hofmann, S. Understanding and Controlling Cu-Catalyzed Graphene Nucleation: The Role of Impurities, Roughness, and Oxygen Scavenging. *Chem. Mater.* **2016**, *28*, 8905.
- (59) Ferrari, A. C.; Meyer, J. C.; Scardaci, V.; Casiraghi, C.; Lazzeri, M.; Mauri, F.; Piscanec, S.; Jiang, D.; Novoselov, K. S.; Roth, S.; Geim, A. K. Raman Spectrum of Graphene and Graphene Layers. *Phys. Rev. Lett.* **2006**, *97*, 187401.
- (60) Ferrari, A. C.; Basko, D. M. Raman Spectroscopy as a Versatile Tool for Studying the Properties of Graphene. *Nat. Nanotechnol.* **2013**, *8*, 235–246.
- (61) Lagatsky, A. A.; Sun, Z.; Kulmala, T. S.; Sundaram, R. S.; Milana, S.; Torrisi, F.; Antipov, O. L.; Lee, Y.; Ahn, J. H.; Brown, C. T. A.; Sibbett, W.; Ferrari, A. C. 2μm Solid-State Laser Mode-Locked by Single-Layer Graphene. *Appl. Phys. Lett.* **2013**, *102*, 013113.
- (62) Das, A.; Pisana, S.; Chakraborty, B.; Piscanec, S.; Saha, S. K.; Waghmare, U. V.; Novoselov, K. S.; Krishnamurthy, H. R.; Geim, A. K.; Ferrari, A. C.; Sood, A. K. Monitoring Dopants by Raman Scattering in an Electrochemically Top-Gated Graphene Transistor. *Nat. Nanotechnol.* **2008**, *3*, 210–215.
- (63) Basko, D. M.; Piscanec, S.; Ferrari, A. C. Electron-Electron Interactions and Doping Dependence of the Two-Phonon Raman Intensity in Graphene. *Phys. Rev. B: Condens. Matter Mater. Phys.* **2009**, *80*, 165413.
- (64) Cançado, L. G.; Jorio, A.; Martins Ferreira, E. H.; Stavale, F.; Achete, C. A.; Capaz, R. B.; Moutinho, M. V. O.; Lombardo, A.; Kulmala, T. S.; Ferrari, A. C. Quantifying Defects in Graphene *via* Raman Spectroscopy at Different Excitation Energies. *Nano Lett.* **2011**, *11*, 3190–3196.
- (65) Bruna, M.; Ott, A. K.; Ijas, M.; Yoon, D.; Sassi, U.; Ferrari, A. C. Doping Dependence of the Raman Spectrum of Defected Graphene. ACS Nano 2014, 8, 7432–7441.
- (66) Ferrari, A. C.; Robertson, J. Interpretation of Raman Spectra of Disordered and Amorphous Carbon. *Phys. Rev. B: Condens. Matter Mater. Phys.* **2000**, *61*, 14095.
- (67) Asuero, A. G.; Sayago, A.; González, A. G. The Correlation Coefficient: An Overview. *Crit. Rev. Anal. Chem.* **2006**, *36*, 41–59.

(68) Lanza, M.; Smets, Q.; Huyghebaert, C.; Li, L.-J. Yield, Variability, Reliability, and Stability of Two-Dimensional Materials Based Solid-State Electronic Devices. *Nat. Commun.* **2020**, *11*, 5689. (69) Langford, E. Quartiles in Elementary Statistics. *Journal of Statistics Education* **2006**, *14*, 3.